

Signatures of three-state Potts nematicity in spin excitations of the van der Waals antiferromagnet FePSe₃

Weiliang Yao,^{1,2,*} Viviane Peçanha-Antonio,³ Devashibhai Adroja,^{3,4} S. J. Gomez Alvarado,^{1,2}
Bin Gao,^{1,2} Sijie Xu,^{1,2} Ruixian Liu,⁵ Xingye Lu,^{5,†} and Pengcheng Dai^{1,2,‡}

¹*Department of Physics and Astronomy, Rice University, Houston, Texas 77005, USA*

²*Rice Laboratory for Emergent Magnetic Materials and Smalley-Curl Institute, Rice University, Houston, Texas 77005, USA.*

³*ISIS Facility, STFC, Rutherford Appleton Laboratory,
Chilton, Didcot, Oxfordshire OX11 0QX, United Kingdom*

⁴*Highly Correlated Matter Research Group, Physics Department,
University of Johannesburg, Auckland Park 2006, South Africa*

⁵*Center for Advanced Quantum Studies and Department of Physics,
Beijing Normal University, Beijing 100875, People's Republic of China*

(Dated: September 3, 2025)

In two-dimensional (2D) nearly square-lattice quantum materials, electron correlations can induce an electronic nematic phase with twofold rotational (C_2) symmetry that profoundly impacts their properties. For 2D materials with threefold rotational (C_3) symmetry, such as the honeycomb lattice, a vestigial three-state Potts nematic order has been observed in the van der Waals antiferromagnet (AFM) FePSe₃ via optical and thermodynamic methods under uniaxial strain. Here, we use neutron scattering to study the magnetic order and spin excitations of FePSe₃ under uniaxial strain. In the AFM ordered state, we find that $\sim 0.6\%$ tensile strain significantly suppresses one zigzag domain and promotes the other two, lowering the AFM order and spin waves to C_2 symmetry. The broken C_3 symmetry in spin excitations persists slightly above $T_N \approx 108.6$ K, where the zigzag AFM order is absent. Our results thus provide direct evidence of magnetoelastic coupling and suggest that the three-state Potts nematicity in paramagnetic spin excitations arises from the vestigial order associated with the low-temperature zigzag AFM order.

Symmetry breaking, such as the formation of new magnetic, structural, or electronic orders, is a fundamental phenomenon in nature. Understanding the nature of symmetry breaking can provide crucial insights into the underlying laws that govern the physical properties of materials [1]. In periodic crystalline solids, rotational symmetry refers to the property that the material remains invariant under rotation by a specific angle. Owing to translational symmetry, crystalline solids can only host twofold, threefold, fourfold, or sixfold discrete rotational symmetries, denoted as C_2 , C_3 , C_4 , and C_6 , respectively [2].

A nematic phase originates from a state where elongated molecules in liquid crystals exhibit no crystalline positional order but are aligned with their long axes approximately parallel, forming directional order with C_2 symmetry [3]. In liquid crystals, it is an intermediate phase between an ordered crystalline solid and a disordered liquid [3]. An electronic nematic phase, predicted to occur near a two-dimensional (2D) nearly square-lattice Mott insulator [4], typically breaks the C_4 symmetry of the underlying lattice and arises near a superconducting phase [5–9]. Since its discovery in copper- and iron-based high-temperature superconductors with nearly square-lattice structures [10, 11], studies of nematicity have often focused on the spontaneous reduc-

tion of C_4 symmetry to C_2 in transport, electronic, and magnetic properties, implying that the system selects one of two energetically equivalent configurations (Ising nematicity) [5–9].

For crystalline solids with C_3 or C_6 symmetry [12], it is also possible to develop a nematic state that selects one (or two) out of three equivalent configurations—a phenomenon known as three-state Potts nematicity [13–15]. Materials in the hexagonal crystal family are thus an ideal platform to explore this type of symmetry breaking. Recent studies on systems with triangular, kagome, and honeycomb lattices have reported intriguing nematic behaviors in their electronic and/or magnetic properties, including Fe_{1/3}NbS₂ [16], Co_{1/3}TaS₂ [17, 18], CsV₃Sb₅ [19–21], ScV₆Sn₆ [22], FePSe₃ [23, 24], and NiPS₃ [25]. However, studies to date have used optical, transport, or thermodynamic methods, which cannot directly probe the microscopic origin of the C_3 symmetry breaking in the nematic phase or determine the energy scale of the corresponding nematic fluctuations.

In this work, we focus on the van der Waals antiferromagnet FePSe₃, which crystallizes in a rhombohedral $R\bar{3}$ structure consisting of hexagonal layers stacked along the c axis through weak van der Waals interactions [Fig. 1(a)] [26, 27]. The Fe ions, with localized magnetic moments, form a honeycomb lattice [Fig. 1(b)] that develops long-range antiferromagnetic (AFM) order below $T_N \approx 108$ K [23, 24, 28, 29]. Neutron diffraction experiments identified a zigzag magnetic structure with propagation wave vector $\mathbf{k}_m = (0.5, 0, 0.5)$ and revealed the weakly first-order nature of the AFM transition, consis-

* wy28@rice.edu

† luxy@bnu.edu.cn

‡ pdai@rice.edu

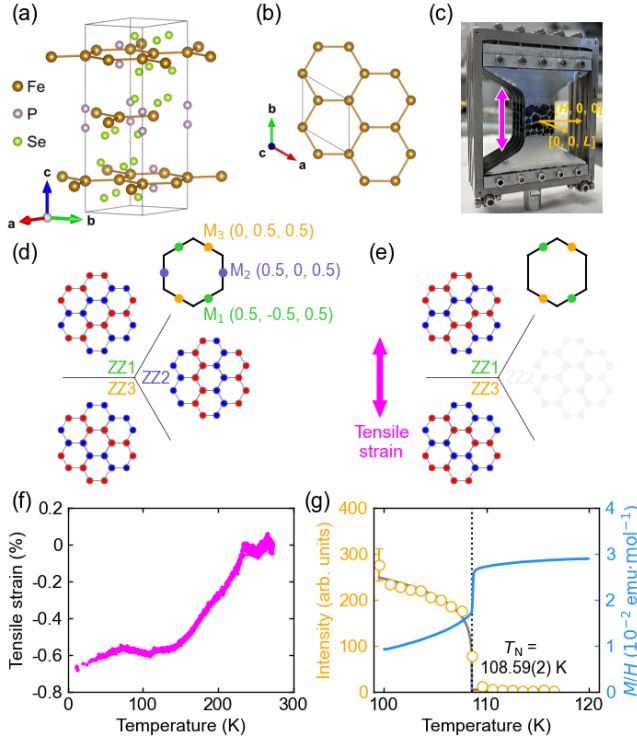


FIG. 1. (a) Crystal structure of FePSe_3 . (b) Honeycomb lattice formed by Fe ions. (c) Strain device with FePSe_3 single crystals attached. The magenta double arrow indicates the tensile strain direction. (d) Three zigzag domains (ZZ1, ZZ2, and ZZ3) in the unstrained Fe honeycomb lattice, where red and blue represent spins pointing into and out of the honeycomb plane. The inset (upper right) shows the six magnetic Bragg peaks in the hexagonal Brillouin zone corresponding to the three zigzag domains. (e) Two remaining zigzag domains (ZZ1 and ZZ3) under tensile strain. (f) Temperature dependence of the tensile strain applied to FePSe_3 single crystals [33]. (g) Temperature dependence of the diffraction intensity at Bragg peak $(0, 0.5, 0.5)$ (left axis) and the magnetic susceptibility under a 0.5 T c -axis field (right axis). The gray solid curve is a power-law fit to the diffraction data, as described in the text. The dashed vertical line marks T_N .

tent with heat-capacity measurements [30–32]. Due to the intrinsic C_3 symmetry of the honeycomb lattice, there are three possible zigzag domains [ZZ1, ZZ2, and ZZ3 in Fig. 1(d)]. In neutron diffraction, ZZ1, ZZ2, and ZZ3 domains contribute to magnetic Bragg peaks at the three M -points of the hexagonal Brillouin zone [M_1 , M_2 , and M_3 in the inset of Fig. 1(d)]. Therefore, one can use the Bragg peak intensities to directly monitor the populations of these zigzag domains.

Recent optical linear dichroism (LD) and elastocaloric measurements have revealed a novel nematic state in FePSe_3 , in which the C_3 lattice symmetry gives rise to a three-state Potts nematicity associated with the underlying AFM order [23, 24]. Without externally applied uniaxial strain, the three equally populated zigzag domains below T_N constitute a three-state Potts state. In-situ uniaxial strain was used to tune this three-state Potts

state and extract the corresponding susceptibility, which exhibits divergent behavior near T_N , indicating the formation of a three-state Potts nematic state [23]. Since FePSe_3 is an AFM insulator, the nematicity is solely related to the spin degrees of freedom. FePSe_3 therefore offers a unique opportunity to study the physics of three-state Potts nematicity arising from spin interactions. While LD and elastocaloric measurements can provide useful information on the three-state Potts nematic phase, they are not microscopic probes and thus cannot unveil the wave vector of the magnetic order or the momentum dependence of the spin dynamics in the nematic state. In copper- and iron-based high-temperature superconductors [10, 35], anisotropic spin excitations in momentum space detected by inelastic neutron scattering (INS) experiments provided direct proof of the nematic state and its connection with anisotropic transport and electronic properties [6–9].

To study possible nematic spin excitations in FePSe_3 , we conducted INS experiments on FePSe_3 single crystals under the application of uniaxial strain, which allows direct control over the populations of different zigzag domains. For a magnet with a strongly first-order AFM transition, critical spin fluctuations around T_N are typically absent, resulting in no or only weak nematic behavior. In contrast, for a weakly first-order AFM transition, uniaxial strain can enhance critical spin fluctuations near the AFM transition regime, thereby promoting a nematic phase, as observed in weakly first-order AFM BaFe_2As_2 [36–38] and strongly first-order AFM SrFe_2As_2 [39]. In the case of unstrained FePSe_3 , the weakly first-order nature of the AFM transition [30, 32] suggests that static magnetic order and spin excitations should obey C_3 symmetry, consistent with the underlying honeycomb lattice. However, when uniaxial strain detwines the three magnetic domains, C_2 -symmetric diffraction and spin-wave patterns are expected below T_N . When the system is warmed above T_N with suppressed static magnetic order, the spin excitations should become gapless immediately with the C_3 symmetry if there are no critical spin fluctuations or a nematic phase. Conversely, if the restoration of the C_3 symmetry is delayed until several K above T_N , the C_2 -symmetric spin excitations in the paramagnetic state would be a signature of the underlying three-state Potts nematicity appearing at temperatures above T_N .

We utilized a novel uniaxial strain device previously used to detwin FeSe single crystals, in which thin aluminum plates are mounted onto the invar alloy frames to induce weakly temperature-dependent uniaxial tensile strain [40]. About 1 gram of FePSe_3 single crystals were co-aligned and attached to the thin aluminum plates of the strain device, with the crystallographic $(H, 0, L)$ plane placed in the horizontal scattering plane [Fig. 1(c)]. When cooling down to below 150 K, a uniaxial tensile strain of about 0.6% is applied along the $[-0.5K, K, 0]$ direction (*i.e.*, perpendicular to the nearest Fe-Fe bond) [Fig. 1(f)], which was determined by in-situ strain-gauge measurements [33, 41]. Our INS experiment using this

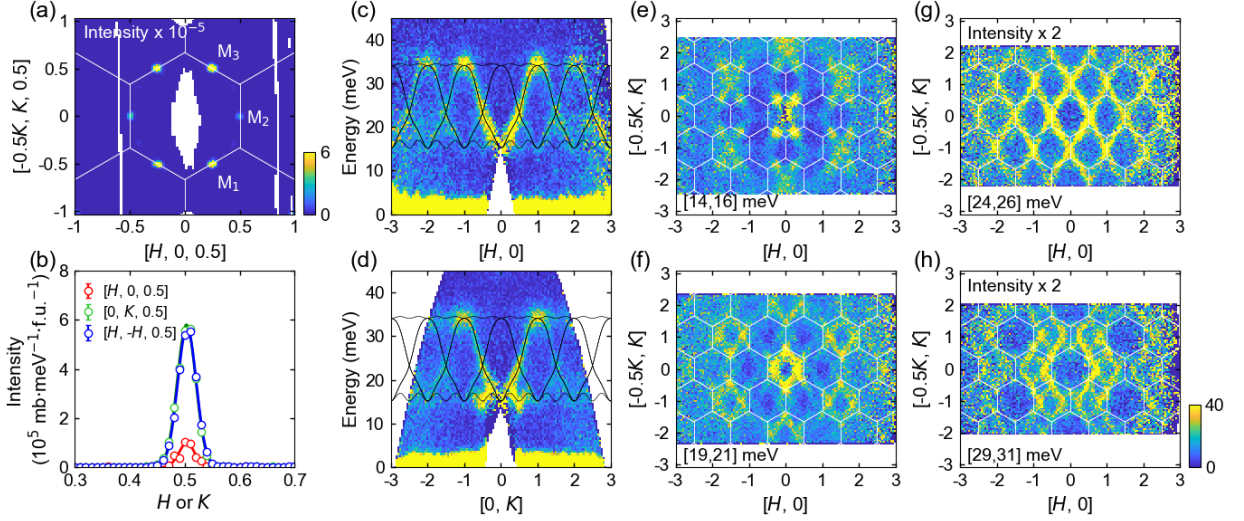


FIG. 2. (a) Elastic scattering pattern of the $(H, K, 0.5)$ plane at 6.0 K. White solid lines mark Brillouin zone boundaries. f.u.: formula unit. (b) Momentum dependence of the intensities around three magnetic Bragg peaks [M_2 , M_3 , and M_1 in the inset of Figs. 1(d) and 1(e)] along $[H, 0, 0.5]$, $[0, K, 0.5]$, and $[H, -H, 0.5]$. Solid curves are Gaussian fits. (c) and (d) Magnetic excitation spectra along $[H, 0]$ and $[0, K]$ at 6.0 K. Black solid curves are calculated spin-wave dispersions using SpinW [34]. (e)-(h) Constant-energy slices of the spectra around 15 meV, 20 meV, 25 meV, and 30 meV at 6.0 K.

strain device was conducted on the time-of-flight spectrometer MERLIN [42] at the ISIS neutron and muon source, Rutherford Appleton Laboratory, UK. More details of the experiment and data analysis can be found in [41].

Figure 1(g) presents the temperature dependence of the intensity at the magnetic Bragg peak M_2 (0, 0.5, 0.5) under uniaxial strain, which shows a typical order-parameter behavior. By fitting the data with a power-law function $I = A(T - T_N)^{2\beta} + B$ (A and B are the scale and background constants, respectively, and β is the critical exponent of the order parameter), we find $T_N = 108.59(2)$ K and $\beta = 0.10(1)$. The obtained T_N coincides with the sharp magnetic susceptibility anomaly in the unstrained case [Fig. 1(g)], which confirms that the transition temperature is unchanged by the uniaxial strain. However, the critical exponent becomes closer to the limit of the 2D Ising model ($\beta = 1/8$) [30], suggesting the magnetic phase transition approaches second order under uniaxial strain, similar to previous works on BaFe_2As_2 [36–38].

A diffraction pattern of the $(H, K, 0.5)$ plane at 6.0 K is shown in Fig. 2(a), from which we find that M_1 and M_3 basically have the same intensity while M_2 is much weaker. Since our sample consists of many co-aligned single crystals [Fig. 1(c)] [41], we expect the three zigzag domains to be present in equal quantities without the strain [30]. Our observation thus suggests that the ZZ2 domain is strongly suppressed by the uniaxial strain, and the ZZ1 and ZZ3 domains are favored [see Fig. 1(e)]. Such strain control of the zigzag domains is consistent with previous reports based on optical methods [23, 24]. By extracting the integrated Bragg peak intensities of M_1 , M_2 , and M_3 (I_{M1} , I_{M2} , and I_{M3}) [Fig. 2(b)], we

estimate a detwinning ratio of $\eta = \frac{(I_{M1} + I_{M3})/2 - I_{M2}}{(I_{M1} + I_{M3})/2 + I_{M2}} \approx 75.7\%$, which is comparable with the experiment on FeSe [40].

Next, we turn to the strain effect on the magnetic excitation spectra. Since FePSe_3 is a quasi-2D antiferromagnet with interlayer exchange interactions much weaker than intralayer ones [30], we integrated over a wide range of L and present the spectra within the honeycomb plane [41]. Spin waves along the $[H, 0]$ and $[0, K]$ directions at 6.0 K are shown in Figs. 2(c) and 2(d), respectively. While the overall dispersions are similar for the two directions, the intensity distributions (dynamic structure factors) exhibit a clear difference. In particular, the low-lying spin-wave branch around 16 meV is strongly suppressed along $[H, 0]$, suggesting that this branch is associated with ZZ2 domain [41] and that low-energy spin excitations are more susceptible to external perturbations. Nevertheless, the measured dispersions can still be well described by previously determined parameters within linear spin-wave theory [Figs. 2(c) and 2(d)] [30], indicating that the exchange interactions remain essentially unchanged under $\sim 0.6\%$ tensile strain and that zigzag domain repopulation is the dominant effect. Constant-energy slices in Figs. 2(e)-(h) further demonstrate that the system exhibits C_2 symmetry at low temperature, consistent with the pronounced optical LD signals [23, 24].

On warming to 108.8 K, which is slightly above T_N , sharp spin waves completely disappear and the broad excitations shift to lower energies [Figs. 3(a) and 3(b)]. Despite very similar spectra along the $[H, 0]$ and $[0, K]$ directions, spin excitations along the $[H, 0]$ direction are overall broader than those along the $[0, K]$ direction.

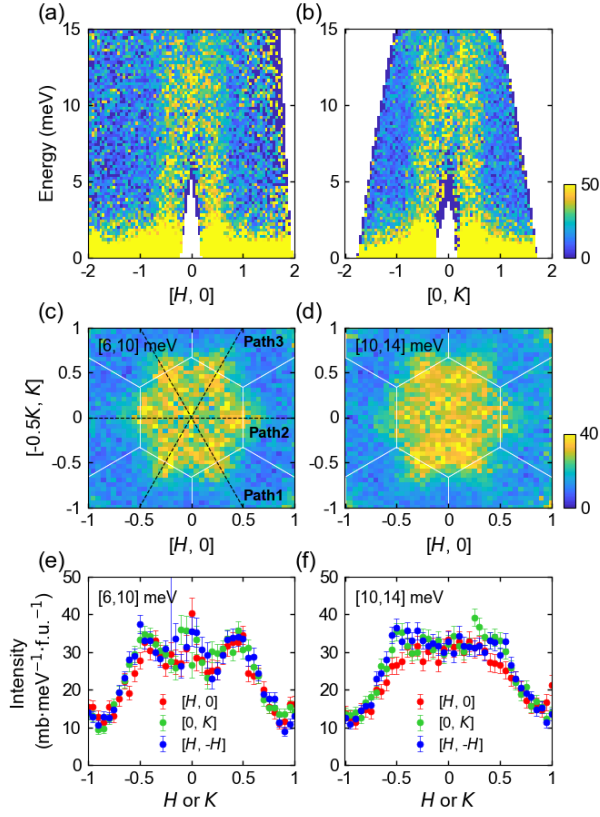


FIG. 3. (a) and (b) Spin excitation spectra along $[H, 0]$ and $[0, K]$ at 108.8 K. (c) and (d) Constant-energy slices of the excitation spectra around 8 meV and 12 meV at 108.8 K. (e) and (f) Momentum dependence of the intensities around 8 meV and 12 meV along $[H, 0]$, $[0, K]$, and $[H, -H]$ [paths 2, 3, and 1 in (c), respectively].

Figures 3(c) and 3(d) present the constant-energy slices taken around 8 meV and 12 meV, respectively. While the intensity distribution in the hexagonal Brillouin zone shows nearly C_3 symmetry around 8 meV, violation of it is evident for the pattern around 12 meV, which is C_2 -symmetric about the c axis. The breaking of the C_3 symmetry can be more clearly seen from the momentum dependence of the intensity, as shown in Figs. 3(e) and 3(f). Around 12 meV, the intensities along the $[0, K]$ and $[H, -H]$ directions are essentially the same, but they deviate from those along the $[H, 0]$ direction near the M points of the Brillouin zone [H or $K = 0.5$ in Fig. 3(f)] by approximately $10 \text{ mb}\cdot\text{meV}^{-1}\cdot\text{f.u.}^{-1}$. These observations suggest the spin fluctuations of FePSe_3 show nematicity without the presence of long-range magnetic order.

The C_3 symmetry of the spin excitation spectra is gradually restored at higher temperatures (109.5 K and 113.0 K), as can be seen in Figures 4(a)-(d). To show the evolution of the C_3 symmetry breaking (or nematicity) above T_N , we use the intensity difference $\Delta I(\mathbf{Q})$, which is defined as $\Delta I(\mathbf{Q}) = [I_1(\mathbf{Q}) + I_3(\mathbf{Q})]/2 - I_2(\mathbf{Q})$, where $I_1(\mathbf{Q})$, $I_2(\mathbf{Q})$, and $I_3(\mathbf{Q})$ are the intensity distributions along the paths 1, 2, and 3 shown in Fig. 3(c). We note

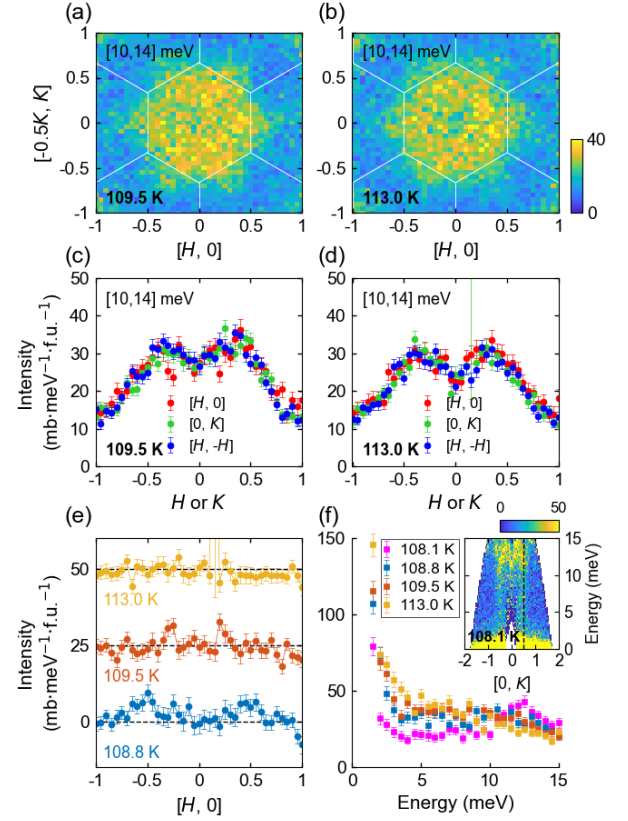


FIG. 4. (a) and (b) Constant-energy slices of the spin excitation spectra around 12 meV at 109.5 K and 113.0 K. (c) and (d) Momentum dependence of the intensities around 12 meV along $[H, 0]$, $[0, K]$, and $[H, -H]$ at 109.5 K and 113.0 K. (e) Momentum dependence of the intensity difference (see text) around 12 meV. Data from different temperatures are evenly offset for clarity. Horizontal dashed lines indicate zero intensity for each temperature. (f) Energy dependence of the intensities around $(0, 0.5)$ at 108.1 K, 108.8 K, 109.5 K, and 113.0 K. Inset shows the spin excitation spectrum along $[0, K]$ at 108.1 K. The vertical dashed line marks $(0, 0.5)$.

that, for strictly C_3 -symmetric spin excitations, $\Delta I(\mathbf{Q}) = 0$. Therefore, this quantity can measure the C_3 symmetry breaking and may be regarded as an effective nematic order parameter [5]. The $\Delta I(\mathbf{Q})$ at three temperatures is presented in Fig. 4(e), where it is nonzero at 108.8 K and 109.5 K, and finally dies away at 113.0 K. The complete disappearance of the C_3 symmetry breaking at 113.0 K also suggests that the feature observed at lower temperatures is not simply due to the applied strain (*e.g.*, mechanical effects) but is intrinsic to the magnetic response. The quick decay of the nematic signal above T_N is consistent with the hyperbola behavior (with respect to temperature) of the nematic susceptibility determined previously [23]. With increasing strain, the AFM transition becomes more second-order-like, thus increasing the critical regime as shown in [23]. For the level of strain we applied ($\sim 0.6\%$), the nematic and AFM transition temperatures are expected to nearly merge together [23],

thus giving rise to the narrow temperature regime above T_N where the C_3 -symmetry-breaking spin excitations are observed.

To further check the characteristics of the spin excitations near T_N , we show the energy dependence of the intensity at $(0, 0.5)$ in Fig. 4(f). At 108.1 K (slightly below T_N), an energy gap of ~ 13 meV can be resolved, signifying the Ising anisotropy of the spin waves [see also in the inset of Fig. 4(f)]. However, the energy gap fully closes at 108.8 K and above. This suggests the nematic spin excitations we observed are in the paramagnetic state, which differs from the anisotropic spin waves below T_N due to the detwinning of zigzag domains. Therefore, the nematic spin excitations slightly above T_N , a hallmark of the three-state Potts nematic state, are a vestigial order for the zigzag AFM order below T_N , and likely arise from strain-induced nematic phase similar to iron pnictides [6–9].

Our experimental results unveil the following sequences of the magnetic phases in FePSe₃. On cooling from the high-temperature paramagnetic spin-disordered state, the system first enters the uniaxial strain-induced three-state Potts nematic state, where the spin excitations are still highly fluctuating but show anisotropy in reciprocal space due to spin-lattice coupling. In the absence of external strain, the nematic order exhibits equal probability along the three equivalent directions of the honeycomb lattice, which hence leads to the C_3 -symmetric excitation patterns as observed previously [30]. When the external strain is applied to induce a tiny lattice distortion, it disfavors the nematic director perpendicular to the strain direction [23, 24]. Due to the divergent nature of the nematic susceptibility, the strain effect is most pronounced close to T_N [23], which results in the C_2 -symmetric excitation pattern. At temperatures lower than T_N , the long-range zigzag AFM order condenses mainly around the M -points where the nematic fluctuations are most significant, and finally establishes the two preferred zigzag domains of dominant population.

The nematic spin excitations observed in FePSe₃ are reminiscent of those in iron-based superconductors such as BaFe_{2-x}Ni_xAs₂ [35] and FeSe [40, 43]. In these systems, the C_4 symmetry of the paramagnetic spin excitations becomes C_2 symmetry in the magnetic ordered state due to orthorhombic lattice distortion and collinear AFM order along the a axis of the orthorhombic lattice [8]. On warming to the paramagnetic tetragonal state

slightly above T_N , spin excitations are C_4 -symmetric without uniaxial strain. However, when a uniaxial strain is applied along one of the tetragonal axis, the low-energy spin excitations become anisotropic along the $[H, 0]$ and $[0, K]$ directions in the 2D square Brillouin zone over a broad range above T_N , forming a strain-driven nematic phase [35, 40, 43]. In contrast, the uniaxial strain induced spin excitation anisotropy in FePSe₃ form in an extremely narrow regime above T_N before becoming isotropic in reciprocal space. This is most likely due to the fact that the AFM phase transition under uniaxial strain is still first-order-like with a narrow critical temperature regime and weak critical spin fluctuations. In addition, while the nematic phase in iron-based superconductors is clearly associated with tetragonal-to-orthorhombic lattice distortion [6–9], there is no known lattice distortion associated with the AFM phase transition in FePSe₃ [30, 31], suggesting that magnetoelasticity may not drive the order-disorder phase transition [44]. Nevertheless, the fact that a uniaxial tensile strain of about 0.6% induces anisotropy in paramagnetic spin excitations of FePSe₃ suggests a small but finite magnetoelastic coupling.

In summary, by performing INS experiments on FePSe₃ single crystals under uniaxial tensile strain, we have mapped out the spin excitation spectra and studied their evolution with temperature. Although the applied strain is only about $\sim 0.6\%$, we observed a significant detwinning effect of the zigzag domains in the AFM ordered state and the corresponding spin waves featuring C_2 symmetry. Moreover, in the paramagnetic state just above the ordering temperature, the spin excitations still exhibit broken C_3 symmetry in a narrow temperature regime, suggesting the presence of magnetoelastic coupling and the underlying three-state Potts nematicity in the spin excitation spectra of FePSe₃.

The neutron scattering work at Rice is supported by the United States Department of Energy, Basic Energy Sciences, DE-SC0012311 (P.D.). The single-crystal growth work at Rice is supported by the Robert A. Welch Foundation under grant no. C-1839 (P.D.). X.L. at BNU is supported by the Scientific Research Innovation Capability Support Project for Young Faculty (Grant No. 2251300009). The experiment at the ISIS Neutron and Muon Source was supported by a beam time allocation RB2510117 from the Science and Technology Facilities Council.

-
- [1] A. J. Beekman, L. Rademaker, and J. van Wezel, *SciPost Phys. Lect. Notes*, **11** (2019).
 - [2] N. W. Ashcroft and N. D. Mermin, *Solid State Physics* (Holt-Saunders, New York, 1976).
 - [3] P.-G. De Gennes and J. Prost, *The physics of liquid crystals*, 83 (Oxford University Press, 1993).
 - [4] S. A. Kivelson, E. Fradkin, and V. J. Emery, *Nature*

393, 550 (1998).

- [5] E. Fradkin, S. A. Kivelson, M. J. Lawler, J. P. Eisenstein, and A. P. Mackenzie, *Annu. Rev. Condens. Matter Phys.* **1**, 153 (2010).
- [6] R. M. Fernandes, P. P. Orth, and J. Schmalian, *Annual Review of Condensed Matter Physics* **10**, 133 (2019).
- [7] L. Nie, G. Tarjus, and S. A. Kivelson, *Proceedings of*

- the National Academy of Sciences **111**, 7980 (2014).
- [8] P. Dai, *Rev. Mod. Phys.* **87**, 855 (2015).
 - [9] A. E. Böhrer, J.-H. Chu, S. Lederer, and M. Yi, *Nature Physics* **18**, 1412 (2022).
 - [10] V. Hinkov, D. Haug, B. Fauqué, P. Bourges, Y. Sidis, A. Ivanov, C. Bernhard, C. T. Lin, and B. Keimer, *Science* **319**, 597 (2008).
 - [11] J.-H. Chu, J. G. Analytis, K. D. Greve, P. L. McMahon, Z. Islam, Y. Yamamoto, and I. R. Fisher, *Science* **329**, 824 (2010).
 - [12] In two-dimensional systems of interest, the C_6 group can be generated by the C_3 and C_2 subgroups. Since the nematic state retains C_2 symmetry, the distinctions between C_3 and C_6 symmetries become irrelevant, rendering them effectively equivalent in this context.
 - [13] R. M. Fernandes and J. W. F. Venderbos, *Science Advances* **6**, eaba8834 (2020).
 - [14] A. R. Chakraborty and R. M. Fernandes, *Phys. Rev. B* **107**, 195136 (2023).
 - [15] Y. Xie, A. Hardy, and A. Paramakanti, *Phys. Rev. B* **110**, 165158 (2024).
 - [16] A. Little, C. Lee, C. John, S. Doyle, E. Maniv, N. L. Nair, W. Chen, D. Rees, J. W. Venderbos, R. M. Fernandes, J. G. Analytis, and J. Orenstein, *Nature Materials* **19**, 1062 (2020).
 - [17] Z. Feng, W. Lu, T. Lu, F. Liu, J. R. Sheeran, M. Ye, J. Xia, T. Kurumaji, and L. Ye, *arXiv preprint arXiv:2507.05486* (2025).
 - [18] E. Kirstein, P. Park, W. Cho, C. D. Batista, J.-G. Park, and S. A. Crooker, *arXiv preprint arXiv:2507.08148* (2025).
 - [19] L. Nie, K. Sun, W. Ma, D. Song, L. Zheng, Z. Liang, P. Wu, F. Yu, J. Li, M. Shan, D. Zhao, S. Li, B. Kang, Z. Wu, Y. Zhou, K. Liu, Z. Xiang, J. Ying, Z. Wang, T. Wu, and X. Chen, *Nature* **604**, 59 (2022).
 - [20] Y. Xu, Z. Ni, Y. Liu, B. R. Ortiz, Q. Deng, S. D. Wilson, B. Yan, L. Balents, and L. Wu, *Nature physics* **18**, 1470 (2022).
 - [21] T. Asaba, A. Onishi, Y. Kageyama, T. Kiyosue, K. Ohtsuka, S. Suetsugu, Y. Kohsaka, T. Gaggli, Y. Kasahara, H. Murayama, K. Hashimoto, R. Tazai, H. Kontani, B. R. Ortiz, S. D. Wilson, Q. Li, H.-H. Wen, T. Shibauchi, and Y. Matsuda, *Nature Physics* **20**, 40 (2024).
 - [22] C. Farhang, W. R. Meier, W. Lu, J. Li, Y. Wu, S. Mozafari, R. P. Madhugaria, Y. Zhang, D. Mandrus, and J. Xia, *Nature Communications* **16**, 7867 (2025).
 - [23] K. Hwangbo, E. Rosenberg, J. Cenker, Q. Jiang, H. Wen, D. Xiao, J.-H. Chu, and X. Xu, *Nature Physics* **20**, 1888 (2024).
 - [24] Z. Ni, D. S. Antonenko, W. J. Meese, Q. Tian, N. Huang, A. V. Haglund, M. Cothrine, D. G. Mandrus, R. M. Fernandes, J. W. Venderbos, J. W. F. Venderbos, and W. Liang, *arXiv preprint arXiv:2308.07249* (2023).
 - [25] Q. Tan, C. A. Occhialini, H. Gao, J. Li, H. Kitadai, R. Comin, and X. Ling, *Nano Letters* **24**, 7166 (2024).
 - [26] B. Taylor, J. Steger, A. Wold, and E. Kostiner, *Inorganic Chemistry* **13**, 2719 (1974).
 - [27] Q. H. Wang, A. Bedoya-Pinto, M. Blei, A. H. Dismukes, A. Hamo, S. Jenkins, M. Koperski, Y. Liu, Q.-C. Sun, E. J. Telford, H. H. Kim, M. Augustin, U. Vool, J.-X. Yin, L. H. Li, A. Falin, C. R. Dean, F. Casanova, R. F. L. Evans, M. Chshiev, A. Mishchenko, C. Petrovic, R. He, L. Zhao, A. W. Tsien, B. D. Gerardot, M. Brotons-Gisbert, Z. Guguchia, X. Roy, S. Tongay, Z. Wang, M. Z. Hasan, J. Wrachtrup, A. Yacoby, A. Fert, S. Parkin, K. S. Novoselov, P. Dai, L. Balicas, and E. J. G. Santos, *ACS Nano* **16**, 6960 (2022).
 - [28] J. Cui, E. V. Boström, M. Ozerov, F. Wu, Q. Jiang, J.-H. Chu, C. Li, F. Liu, X. Xu, A. Rubio, A. Rubio, and Q. Zhang, *Nature Communications* **14**, 3396 (2023).
 - [29] A. Haglund, *Thermal conductivity of MXY_3 magnetic layered trichalcogenides*, Ph.D. thesis, University of Tennessee, Knoxville, TN (2019), ph.D. dissertation.
 - [30] L. Chen, X. Teng, D. Hu, F. Ye, G. E. Granroth, M. Yi, J.-H. Chung, R. J. Birgeneau, and P. Dai, *npj Quantum Materials* **9**, 40 (2024).
 - [31] A. Wiedenmann, J. Rossat-Mignod, A. Louisy, R. Brec, and J. Rouxel, *Solid State Communications* **40**, 1067 (1981).
 - [32] A. Bhutani, J. L. Zuo, R. D. McAuliffe, C. R. dela Cruz, and D. P. Shoemaker, *Phys. Rev. Mater.* **4**, 034411 (2020).
 - [33] Z. Mo, C. Li, W. Zhang, C. Liu, Y. Sun, R. Liu, and X. Lu, *Chinese Physics Letters* **41**, 107102 (2024).
 - [34] S. Toth and B. Lake, *Journal of Physics: Condensed Matter* **27**, 166002 (2015).
 - [35] X. Lu, J. T. Park, R. Zhang, H. Luo, A. H. Nevidomskyy, Q. Si, and P. Dai, *Science* **345**, 657 (2014).
 - [36] M. G. Kim, R. M. Fernandes, A. Kreyssig, J. W. Kim, A. Thaler, S. L. Bud'ko, P. C. Canfield, R. J. McQueeney, J. Schmalian, and A. I. Goldman, *Phys. Rev. B* **83**, 134522 (2011).
 - [37] X. Lu, K.-F. Tseng, T. Keller, W. Zhang, D. Hu, Y. Song, H. Man, J. T. Park, H. Luo, S. Li, A. H. Nevidomskyy, and P. Dai, *Phys. Rev. B* **93**, 134519 (2016).
 - [38] P. Liu, M. L. Klemm, L. Tian, X. Lu, Y. Song, D. W. Tam, K. Schmalzl, J. Park, Y. Li, G. Tan, Y. Su, F. Bourdarot, Y. Zhao, J. W. Lynn, R. J. Birgeneau, and P. Dai, *Nature Communications* **11**, 5728 (2020).
 - [39] D. W. Tam, W. Wang, L. Zhang, Y. Song, R. Zhang, S. V. Carr, H. C. Walker, T. G. Perring, D. T. Adroja, and P. Dai, *Phys. Rev. B* **99**, 134519 (2019).
 - [40] R. Liu, M. B. Stone, S. Gao, M. Nakamura, K. Kamazawa, A. Krajewska, H. C. Walker, P. Cheng, R. Yu, Q. Si, P. Dai, and X. Lu, *Nature Communications* **16**, 5212 (2025).
 - [41] See Supplemental Material [url] for additional data and analyses.
 - [42] R. Bewley, R. Eccleston, K. McEwen, S. Hayden, M. Dove, S. Bennington, J. Treadgold, and R. Coleman, *Physica B: Condensed Matter* **385-386**, 1029 (2006).
 - [43] X. Lu, W. Zhang, Y. Tseng, R. Liu, Z. Tao, E. Paris, P. Liu, T. Chen, V. N. Strocov, Y. Song, R. Yu, Q. Si, P. Dai, and T. Schmitt, *Nature Physics* **18**, 806 (2022).
 - [44] H. Lane and M. Mourigal, *Phys. Rev. B* **111**, 174446 (2025).
 - [45] R. Basnet, T. Patel, J. Wang, D. Upreti, S. K. Chhetri, G. Acharya, M. R. U. Nabi, J. Sakon, and J. Hu, *Advanced Electronic Materials* **10**, 2300738 (2024).
 - [46] O. Arnold *et al.*, *Nuclear Instruments and Methods in Physics Research Section A: Accelerators, Spectrometers, Detectors and Associated Equipment* **764**, 156 (2014).
 - [47] R. Ewings, A. Buts, M. Le, J. van Duijn, I. Bustinduy, and T. Perring, *Nuclear Instruments and Methods in Physics Research Section A: Accelerators, Spectrometers, Detectors and Associated Equipment* **834**, 132 (2016).
 - [48] G. Xu, Z. Xu, and J. M. Tranquada, *Review of Scientific Instruments* **84**, 083906 (2013).

Supplemental Material for “Signatures of three-state Potts nematicity in spin excitations of the van der Waals antiferromagnet FePSe₃”

I. FEPSE₃ SINGLE CRYSTAL GROWTH AND CHARACTERIZATION

High-quality FePSe₃ single crystals were synthesized using a chemical vapor transport method. A mixture of 0.52 g iron powder, 0.29 g phosphorus chunks, 2.20 g selenium powder, and 0.25 g iodine was loaded into a quartz tube (outer diameter 35 mm, wall thickness 1.5 mm), which was then evacuated and sealed under vacuum. The sealed portion of the tube was approximately 17 cm in length. The tube was placed in a one-zone furnace with the starting materials positioned at the hot end. Since the central region of the furnace has nearly uniform temperature, the tube was shifted 8 cm away from the center to create a temperature gradient. The furnace was programmed to ramp to 620 °C within 6 hours, held at this temperature for 108 hours, and then switched off. Large FePSe₃ single crystals with a hexagonal morphology were obtained at the cold end of the tube [Fig. S5(a)]. X-ray Laue diffraction [Fig. S5(b)] confirmed that the edge of the hexagonal crystal is perpendicular to the $[H, 0, 0]$ direction. For inelastic neutron scattering (INS) experiments, the FePSe₃ crystals were glued to thin aluminum plates using hydrogen-free CYTOP adhesive. These plates were mounted on invar alloy frames [Fig. S5(c)], where the mismatch in thermal expansion coefficients between the invar alloy frame and the aluminum plate applied a uniaxial tensile strain to the samples upon cooling [40].

The magnitude of the uniaxial tensile strain applied to the FePSe₃ samples was determined using a custom-built cryogenic digital image correlation (CDIC) system [33, 40]. A piece of FePSe₃ single crystal was mounted on a compact strain device of the same design, which is compatible with a low-temperature cryostat equipped with an optical window. The relative displacements between feature points on the sample were tracked during cooling. The effective strain [Fig. 1(f)] was calculated from the difference in distance shifts along and perpendicular to the aluminum plate. More details of this measurement can be found in [40] and [33].

To examine the antiferromagnetic (AFM) phase transition in our FePSe₃ single crystals, we measured the magnetic susceptibility using a Quantum Design PPMS. Fig. S6(a) displays the temperature dependence of the susceptibility under a 0.5 T field applied along both the c axis and the \mathbf{a}^* direction, with a temperature sweep rate of 3 K/min for both cooling and warming. The results are generally consistent with previous reports [24, 45] and indicate an easy-axis spin configuration in the AFM ordered state. A clear thermal hysteresis is observed, as the cooling and warming curves do not overlap. This feature is highlighted in the enlarged view in Fig. S6(b). The Néel temperatures (T_N), defined by the peak positions of the temperature derivative of the susceptibility [Fig. S6(c)], are ~ 106.04 K on cooling and ~ 110.97 K on warming. However, when the sweep rate was reduced to 0.05 K/min, the peak position of $d(M/H)/dT$ shifted to ~ 108.65 K, essentially midway between the two faster-sweep values. This result demonstrates that an accurate determination of T_N requires a slow sweep rate to ensure thermal equilibrium. Notably, the T_N obtained from our neutron diffraction measurement [Fig. 1(g)], 108.59(2) K, agrees very well with the thermally equilibrated result. That slow-sweep measurement took approximately 4 hours to cover the temperature range from ~ 100 K to ~ 117 K.

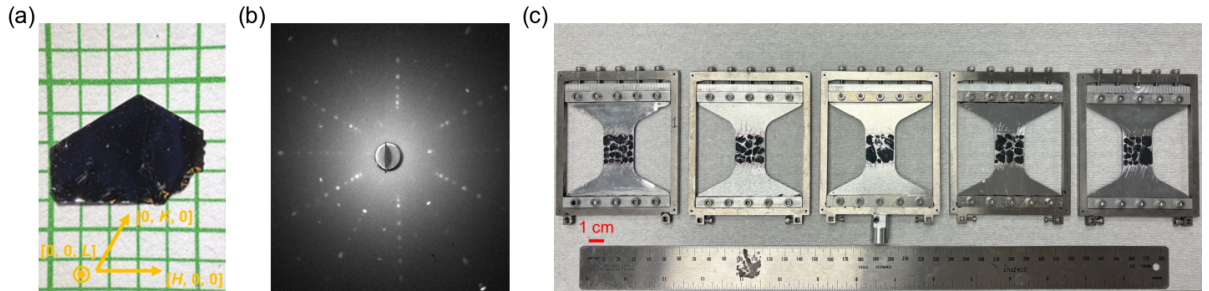


FIG. S5. (a) One piece of representative FePSe₃ single crystal against a millimeter grid. (b) X-ray Laue diffraction pattern taken on the $(0, 0, L)$ surface. Photograph of the disassembled strain device with the FePSe₃ single crystals attached.

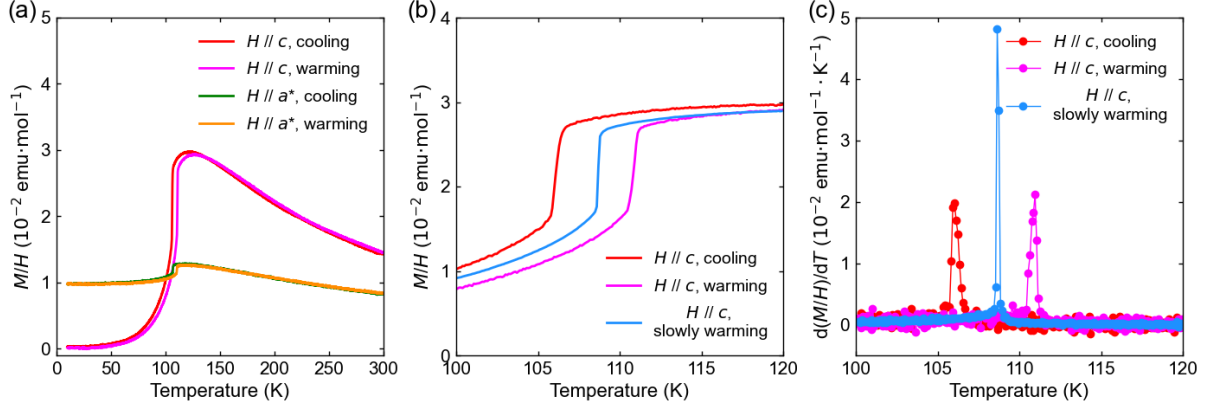


FIG. S6. (a) Temperature dependence of the magnetic susceptibility under a 0.5 T field applied along the c axis and the a^* direction, showing both warming and cooling processes. (b) Enlarged view of the magnetic susceptibility between 100 K and 120 K for the field applied along the c axis. The magnetic susceptibility measured with a much slower temperature sweep rate is also shown. (c) The temperature derivative of the magnetic susceptibility shown in (b).

II. INELASTIC NEUTRON SCATTERING EXPERIMENT AND ADDITIONAL DATA

Our INS experiment was performed with the MERLIN spectrometer. To avoid the large background from the invar frames of the strain device, these frames were covered with cadmium foils before loading into the spectrometer. With MERLIN's repetition-rate multiplication mode, data from three incident neutron energies ($E_i = 61.9$ meV, 21.3 meV, and 11.1 meV) were simultaneously collected. The chopper frequency was set to be 250 Hz. The energy resolutions at zero energy transfer are about 3.5 meV, 0.85 meV, and 0.35 meV for $E_i = 61.9$ meV, 21.3 meV, and 11.1 meV, respectively. We measured at six temperatures (6.0 K, 100.0 K, 108.1 K, 108.8 K, 109.6 K, and 113.0 K) with the sample rotated for 60 degrees along the $[-0.5K, K, 0]$ direction.

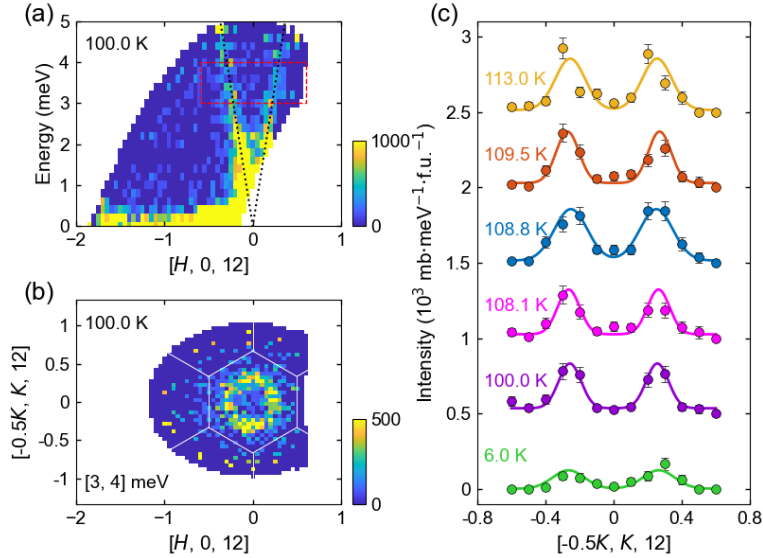


FIG. S7. (a) Acoustic phonon emerging from (0, 0, 12) at 100.0 K. Black dashed lines indicate the linear phonon dispersion. (b) Constant-energy slice of the $(H, K, 12)$ plane around 3.5 meV showing the acoustic phonon. (c) Momentum dependence of the phonon intensity around 3.5 meV along the $[-0.5K, K, 12]$ direction [red dashed box in (a)] for six temperatures. Data are vertically offset by 500 mb-meV $^{-1}$ · f.u. $^{-1}$ for clarity. Solid curves are double-Gaussian fits to the data.

Data reduction was carried out using Mantid [46] and HORACE [47]. Except for the diffraction data in Fig. 1(g), all presented intensities were converted to absolute units of mb-meV $^{-1}$ · f.u. $^{-1}$ using the phonon scattering around (0, 0, 12) (see Fig. S7) following a standard procedure [48]. The momentum- and/or energy-integration ranges and the

incident energies (E_i s) for the presented data are summarized in Table I.

Fig. S8 shows the high-energy spin excitation spectra at six temperatures. Dispersive spin waves are sustained up to 108.1 K, whereas no clear dispersion is discernible at 108.8 K and above. The symmetry of the excitation patterns is examined in Fig. S9, which displays constant-energy slices around 25 meV. The thermal evolution of the low-energy excitations is shown in Fig. S10.

III. SPIN WAVES FROM DIFFERENT ZIGZAG ANTIFERROMAGNETIC DOMAINS

For unstrained FePSe_3 , three zigzag domains coexist in the AFM ordered state [ZZ1, ZZ2, and ZZ3 as shown in Fig. 1(d)]. The spin waves along a given trajectory generally receive contributions from all three domains. Figure S11 shows the calculated spin-wave spectra for ZZ1, ZZ2, and ZZ3 individually. The observed spectrum is a linear combination of these, weighted by the domain population. In our experiment, uniaxial strain strongly suppresses ZZ2 while favoring ZZ1 and ZZ3. Diffraction measurements [Fig. 2(a) and (b)] yield a domain ratio of ZZ1 : ZZ2 : ZZ3 \approx 0.47 : 0.06 : 0.46. Using this distribution, we calculated the spin-wave spectra along the $[H, 0]$ and $[0, K]$ directions (Fig. S12), which reproduce the measured spectra in Fig. 2(c) and (d) with good agreement.

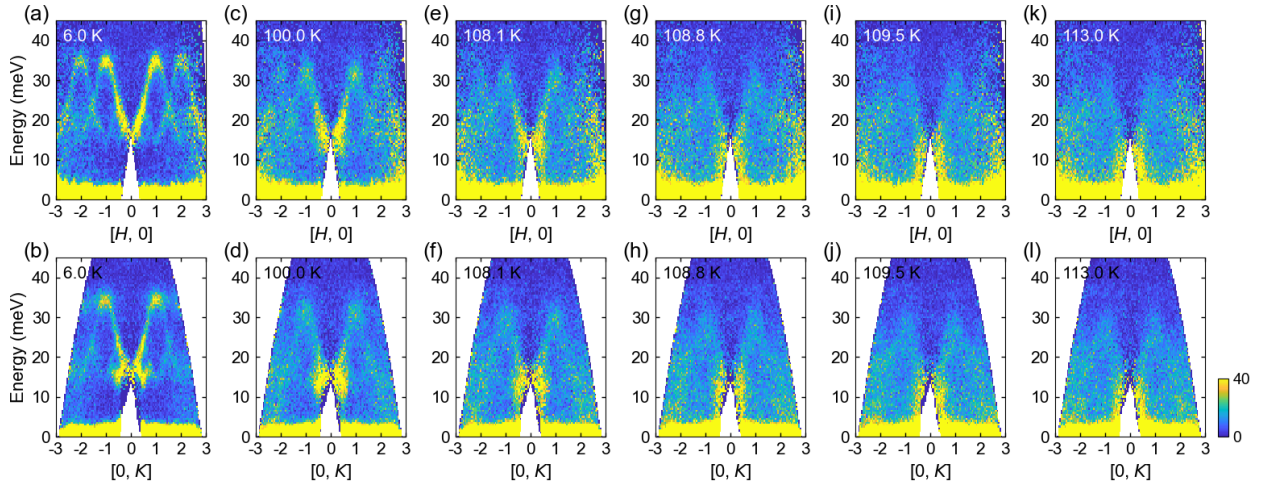


FIG. S8. High-energy spin excitation spectra at six temperatures along $[H, 0]$ [(a), (c), (e), (g), (i), and (k)] and $[0, K]$ [(b), (d), (f), (h), (j), and (l)].

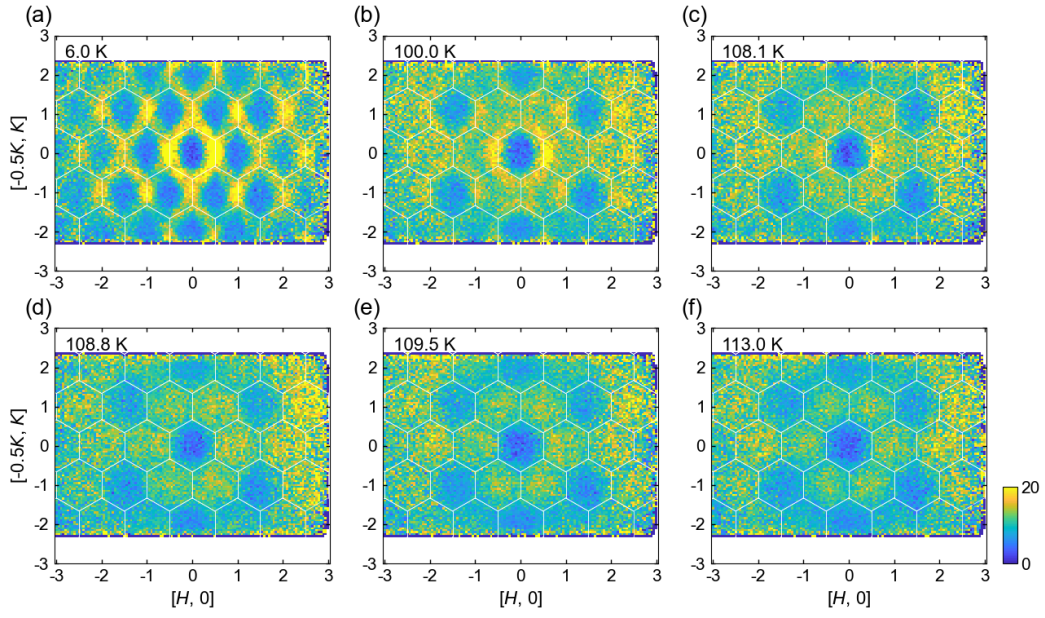


FIG. S9. Constant-energy slices of the spin excitation spectra around 25 meV at six temperatures.

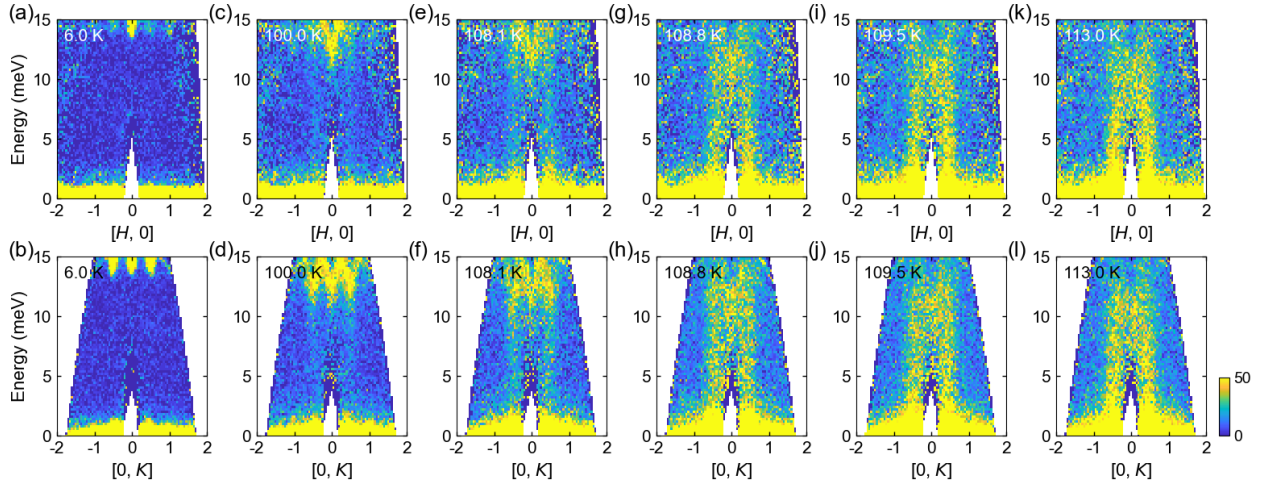


FIG. S10. Low-energy spin excitation spectra at six temperatures along $[H, 0]$ [(a), (c), (e), (g), (i), and (k)] and $[0, K]$ [(b), (d), (f), (h), (j), and (l)].

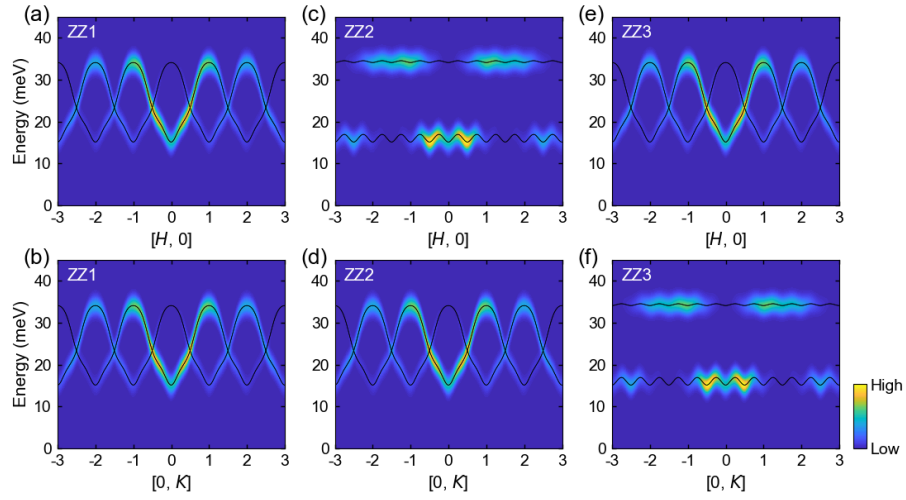


FIG. S11. Calculated spin-wave spectra for the three zigzag domains (ZZ1, ZZ2, and ZZ3) along $[H, 0]$ and $[0, K]$. The black solid curves are the corresponding spin-wave dispersions.

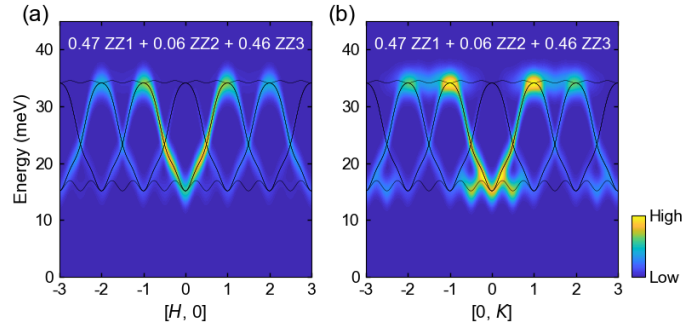


FIG. S12. Calculated spin-wave spectra along $[H, 0]$ and $[0, K]$ based on the domain population determined from the diffraction measurement. The black solid curves are the corresponding spin-wave dispersions.

TABLE I. Momentum- and/or energy-integration ranges and E_i s for the data presented in figures.

Data	Momentum-integration range (r.l.u.)	Energy-integration range (meV)	E_i (meV)
Fig. 2(a)	$[-0.05, 0.05]$ along $[0, 0, L]$	$[-0.5, 0.5]$	11.1
Fig. 2(b)	$[-0.1, 0.1]$ along $[0.5K, -K, 0]$ (red) $[-0.1, 0.1]$ along $[-H, 0.5H, 0]$ (green) $[-0.1, 0.1]$ along $[0.5K, 0.5K, 0]$ (blue) $[-0.05, 0.05]$ along $[0, 0, L]$	$[-0.5, 0.5]$	11.1
Fig. 2(c)	$[-0.1, 0.1]$ along $[0.5K, -K, 0]$ $[-10, 10]$ along $[0, 0, L]$	-	61.9
Fig. 2(d)	$[-0.1, 0.1]$ along $[-H, 0.5H, 0]$ $[-10, 10]$ along $[0, 0, L]$	-	61.9
Fig. 2(e)-(h)	$[-10, 10]$ along $[0, 0, L]$	$[-1, 1]$	61.9
Fig. 3(a)	$[-0.1, 0.1]$ along $[0.5K, -K, 0]$ $[-6, 6]$ along $[0, 0, L]$	-	21.3
Fig. 3(b)	$[-0.1, 0.1]$ along $[-H, 0.5H, 0]$ $[-6, 6]$ along $[0, 0, L]$	-	21.3
Fig. 3(c) and (d)	$[-6, 6]$ along $[0, 0, L]$	$[-2, 2]$	21.3
Fig. 3(e) and (f)	$[-0.1, 0.1]$ along $[0.5K, -K, 0]$ (red) $[-0.1, 0.1]$ along $[-H, 0.5H, 0]$ (green) $[-0.1, 0.1]$ along $[0.5K, 0.5K, 0]$ (blue) $[-6, 6]$ along $[0, 0, L]$	$[-2, 2]$	21.3
Fig. 4(a) and (b)	$[-6, 6]$ along $[0, 0, L]$	$[-2, 2]$	21.3
Fig. 4(c) and (d)	$[-0.1, 0.1]$ along $[0.5K, -K, 0]$ (red) $[-0.1, 0.1]$ along $[-H, 0.5H, 0]$ (green) $[-0.1, 0.1]$ along $[0.5K, 0.5K, 0]$ (blue) $[-6, 6]$ along $[0, 0, L]$	$[-2, 2]$	21.3
Fig. 4(f)	$[-0.1, 0.1]$ along $[H, 0, 0]$ $[-0.1, 0.1]$ along $[0.5K, -K, 0]$ $[-6, 6]$ along $[0, 0, L]$	-	21.3
Fig. 4(f) inset	$[-0.1, 0.1]$ along $[-H, 0.5H, 0]$ $[-6, 6]$ along $[0, 0, L]$	-	21.3
Fig. S7(a)	$[-0.1, 0.1]$ along $[0.5K, -K, 0]$ $[-0.25, 0.25]$ along $[0, 0, L]$	-	11.1
Fig. S7(b)	$[-0.25, 0.25]$ along $[0, 0, L]$	$[-0.5, 0.5]$	11.1
Fig. S7(c)	$[-0.1, 0.1]$ along $[0.5K, -K, 0]$ $[-0.25, 0.25]$ along $[0, 0, L]$	$[3, 4]$	11.1
Fig. S8(a), (c), (e), (g), (i), and (k)	$[-0.1, 0.1]$ along $[0.5K, -K, 0]$ $[-10, 10]$ along $[0, 0, L]$	-	61.9
Fig. S8(b), (d), (f), (h), (j), and (l)	$[-0.1, 0.1]$ along $[-H, 0.5H, 0]$ $[-10, 10]$ along $[0, 0, L]$	-	61.9
Fig. S9	$[-10, 10]$ along $[0, 0, L]$	$[-5, 5]$	21.3
Fig. S10(a), (c), (e), (g), (i), and (k)	$[-0.1, 0.1]$ along $[0.5K, -K, 0]$ $[-6, 6]$ along $[0, 0, L]$	-	21.3
Fig. S10(b), (d), (f), (h), (j), and (l)	$[-0.1, 0.1]$ along $[-H, 0.5H, 0]$ $[-6, 6]$ along $[0, 0, L]$	-	21.3